Force Modeling for Needle Insertion Into Soft Tissue

Allison M. Okamura*, *Member, IEEE*, Christina Simone, and Mark D. O'Leary

Abstract—The modeling of forces during needle insertion into soft tissue is important for accurate surgical simulation, preoperative planning, and intelligent robotic assistance for percutaneous therapies. We present a force model for needle insertion and experimental procedures for acquiring data from *ex vivo* tissue to populate that model. Data were collected from bovine livers using a one-degree-of-freedom robot equipped with a load cell and needle attachment. computed tomography imaging was used to segment the needle insertion process into phases identifying different relative velocities between the needle and tissue. The data were measured and modeled in three parts: 1) capsule stiffness, a nonlinear spring model; 2) friction, a modified Karnopp model; and 3) cutting, a constant for a given tissue. In addition, we characterized the effects of needle diameter and tip type on insertion force using a silicone rubber phantom. In comparison to triangular and diamond tips, a bevel tip causes more needle bending and is more easily affected by tissue density variations. Forces for larger diameter needles are higher due to increased cutting and friction forces.

Index Terms—Biological tissues, modeling, robotics, surgery.

I. INTRODUCTION

MODELING the interaction between surgical tools and deformable tissues based on measurements of real and phantom tissue properties has been the topic of a significant research effort in recent years [1]–[5]. Such models are useful for realistic surgical simulation, preoperative planning, and autonomous and robot-assisted medical procedures. Acquiring data from biological tissues and developing models appropriate for application in simulation or robot-assisted surgery is difficult due to tissue deformation, inhomogeneity, and opacity, as well as the many possible sources of force applied to a surgical tool (i.e., stiffness, friction, and cutting).

Although there are many types of tools used in medical intervention, this paper focuses on percutaneous therapies with needles. Percutaneous therapies are minimally invasive diagnostic or therapy delivery procedures that involve the insertion of tubular delivery devices into targeted locations in the body, typically with the aid of intra-operative imaging. In comparison with open surgery, these techniques reduce patient dis-

comfort and decrease recovery time. However, a major shortcoming is reduced visual and tactile information transmitted to the physician via the instruments. Current clinical methods involve an iterative manual technique of imaging and positioning, which lacks real-time presentation of information to the operator. Complications have arisen due to the imprecise placement of surgical instruments, because incorrect dosage distribution or damage to delicate structures [6]–[8].

In this paper, the liver was chosen as the organ of interest due to its relevance to important percutaneous procedures. The American Cancer Society estimates that 18 920 new cases of primary liver cancer and intrahepatic bile duct cancer will be diagnosed in the United States during 2004 [9]. Liver biopsy, involving the insertion of a biopsy needle to retrieve a sample of tissue, is often used to diagnose the cause and extent of chronic liver disease and diagnose liver tumors identified by imaging tests. Liver biopsy is also used after liver transplantation to determine if rejection is present. An approach to treating liver cancer is ablation, which is also typically performed with needles. While the experiments presented in this paper were performed with bovine liver and silicone rubber with similar properties, the experimental methods could be used with any soft tissue.

This paper is organized as follows. First, we describe related work in the areas of reality-based modeling, tool-tissue interaction modeling, surgical simulation, and the use of tissue models in robot-assisted surgery. Second, we present a set of experiments to characterize the various sources of force arising during needle insertion into liver tissue. Third, we examine the effect of needle properties (diameter and tip type) on insertion forces. Finally, we provide conclusions and directions for future work.

II. RELATED WORK

Reality-based modeling involves the automatic measurement of actual environment properties for the purpose of developing realistic virtual models. We are particularly interested in haptic models, which include relationships between motions and forces during interaction with an object. This manner of identification has been performed for many different types of systems; we provide several examples here. MacLean [10] developed the concept of the "haptic camera," a system that could characterize haptic properties of interactive objects such as switches, and display those properties in a virtual environment. Dupont *et al.* [11] demonstrated that object properties such as dimension, weight and friction could be recorded during teleoperation with haptic feedback to the operator. Okamura *et al.* [12] showed that vibration characteristics of different materials could be acquired through acceleration data, modeled, and then displayed in a virtual environment to enhance operator perception of object hardness. Mahvash and Hayward [13] viewed the cutting of a deformable body using a model of energy exchange. They validated their approach by acquiring

*A. M. Okamura is with the Department of Mechanical Engineering, Johns Hopkins University, 125 Latrobe Hall, 3400 N. Charles Street, Baltimore, MD 21218 USA (e-mail: aokamura@jhu.edu).

C. Simone was with is with Johns Hopkins University, Baltimore, MD 21218 USA. She is now with the Naval Surface Warfare Center, Bethesda, MD 20817 USA (e-mail: christina_simone@yahoo.com).

M. D. O'Leary was with is with Johns Hopkins University, Baltimore, MD 21218 USA. He is now with the Department of Mechanical Engineering, Carnegie Mellon University, Pittsburgh, PA 15213 USA (e-mail: moleary@andrew.cmu.edu).

models from cutting prismatic samples of potato and calf liver with a sharp razor blade, and then displaying the models in a virtual environment.

In recent years there has been burgeoning interest in the modeling of forces resulting from tool-tissue interactions. DiMaio and Salcudean [3], [14] performed pioneering work in modeling and simulating the deformations that occur during needle insertion. A robot instrumented with a force sensor and needle was inserted into phantom tissue, while the deformations were measured via computer vision. The force distribution along the needle shaft was estimated based on observed tissue deformations. Ottensmeyer and Salisbury [5], Brouwer *et al.* [2] and Rosen *et al.* [4] have developed specialized surgical devices that can acquire *in vivo* data for grasping or probing soft tissues. Kataoka *et al.* [15] developed a special tool to separate shaft forces from tip forces during needle insertion, but did not create models from acquired data. A lacuna exists in the current literature regarding explicit experiments and models for the different sources of force during needle insertion into soft tissues.

The force models developed can be used in surgical simulation and robot-assisted surgeries. Although the usage of these models is not a contribution of this paper, we provide some example applications here. A number of researchers have developed haptic virtual environments for surgical simulation, for procedures including brachytherapy [16], catheter insertion [17], lumbar puncture [18], epidural blocks [19], [20], endoscopic surgeries [21], and laparoscopic surgeries [22]. Data acquired from actual tissues can be used to evaluate the accuracy of these simulators and also to populate the models with appropriate material properties. Accurate models are not only important for haptic feedback, but they also determine the way tissue deforms during contact with a surgical tool. In the areas of telemanipulation and human-robot cooperative manipulation, there are only a few examples of reality-based modeling used in medical interventions. Yen *et al.* [23] describe a telemanipulation system for assisting in the penetration of soft tissue for medical tasks. The system interacts with the environment through a rotating arm that performs needle insertion. They construct a simulation using velocity and acceleration information calculated from encoder readings of a single test of a porcine sample. Brett *et al.* [1] presented an automated handheld device to interpret the type and deformation of tissue while being inserted into recently deceased porcine and human lumbar samples. Components measured include syringe pressure, force, and needle displacement. As reality-based tissue models such as those described in this paper improve, we anticipate that they will be used more often in tissue simulation and robot-assisted surgical systems, improving realism and performance.

III. CHARACTERIZATION OF NEEDLE INSERTION FORCES

In order to accurately model the forces resulting from needle insertion, it is necessary to separate force data into components from difference sources. There has been no prior work on the explicit measurement of different force components for the purpose of modeling needle insertion forces. Sample force versus position data acquired during needle insertion into bovine liver (Fig. 1) reveals one primary puncture and subsequent internal punctures. The main puncture event is designated by a peak in
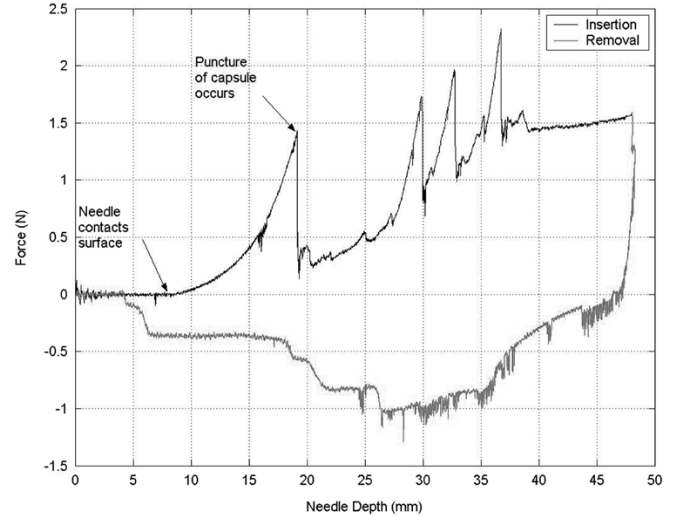
(a)
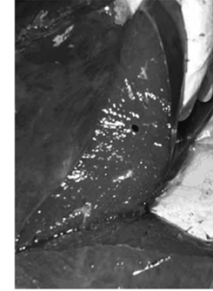
(b)

Fig. 1. (a) Needle axial forces measured during insertion into and removal from bovine liver. The main puncture event occurs at the capsule. (b) Additional puncture events occur due to collisions with internal structures such as those shown in this cut of liver.

force after a steady rise, followed by a sharp decrease. Subsequent variations in force are due to friction, cutting forces, and internal stiffness, as well as collisions with and puncture of interior structures. We note that because the liver functions to filter and process blood, it contains a substantial number of arteries and veins. The structural and functional units of the liver are ∼2 mm, hexagonally-shaped lobules that are comprised of liver cells arranged in one-cell-thick plate-like layers that radiate from the central vein to the edge of the lobule. At each of the six corners of a lobule is a portal triad, consisting of a branch of the hepatic artery, hepatic portal vein, and a bile duct [24]. The internal puncture events (identified by elevated forces and subsequent sudden drops in force) are evident in Fig. 1(a).

The force data collected is a summation of stiffness, friction, and cutting forces

$$f_{\text{needle}}(x) = f_{\text{stiffness}}(x) + f_{\text{friction}}(x) + f_{\text{cutting}}(x). \quad (1)$$

We define these forces such that the stiffness force occurs before puncture of the capsule, and the friction and cutting forces occur after this main puncture. We consider that cutting forces include the plastic deformation from the act of cutting as well as the force resulting from tissue stiffness at the tip of the needle. Likewise, friction force is also a function of the internal stiffness of the tissue. In this section, we present models, experiments and results for characterizing the forces resulting from tissue stiffness, friction, and cutting.
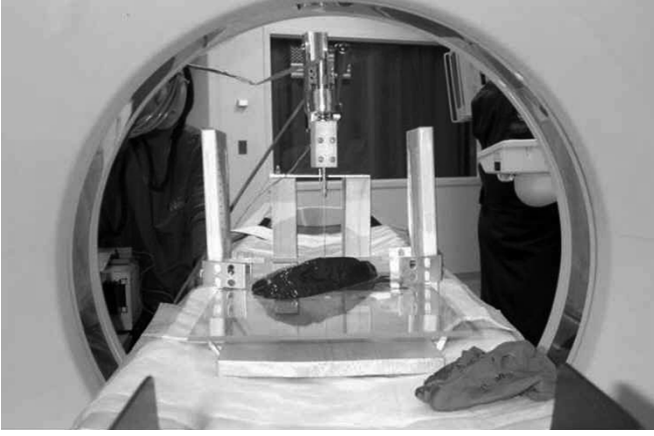
Fig. 2. Experimental setup for data collection under CT flouro imaging. A translational stage controls the motion of the needle. The liver is suspended between two clear acrylic plates, and small holes in the plates allow the needle to pass through.

A. Equipment

Data was acquired using a 1-degree-of-freedom translation stage to guide a 1.27-mm O.D., 15.24-cm-long surgical needle with a bevel tip into bovine liver. The livers were all tested at room temperature within three to six hours after death. A 1-axis 10-N capacity Entran™ load cell was used to measure forces in the direction of motion. The control software executed on a Windows NT Pentium II 450-MHz computer with a graphical user interface. The time, position of the needle, and force were recorded at a frequency of 500 Hz. Imaging data was gathered with a clinical Toshiba Multi-Slice Aquilion 0.5 CT Fluoro™ machine. Fig. 2 shows the setup for experiments performed under computed tomography (CT) fluoroscopy.

B. Tissue Stiffness and Puncture Force

In this experiment, we sought to characterize liver stiffness and primary puncture force. We focus here on the forces applied by the needle before it travels through tissue. Many researchers have addressed external measurement of tissue stiffness, and a number of different nonlinear models have been proposed [3]–[5], [25]. The work described in this section is not a significantly new approach, but it is provided for completeness because prepuncture stiffness is included in the complete needle force model. We note that nonlinearity of force versus displacement data can occur due to both inherent nonlinearity of tissue stiffness properties and the geometry of the tissue. We do not attempt to separate these effects. In addition, the tissue is not preconditioned as is often done in the biomechanics literature [26], since models developed from such data would not accurately reflect the forces occurring during actual interventions.

The stiffness force is due to the elastic properties of the organ and its capsule, and can be identified from prepuncture forces in the insertion data. We performed insertions at a constant velocity of 3 mm/s on two bovine livers (Liver 1 and Liver 2). The force on the needle is described by the relationship

$$f_{\text{stiffness}} = \begin{cases} 0, & z_{\text{tip}} < z_1 \\ f(z), & z_1 \leq z_{\text{tip}} \leq z_2 \\ 0, & z_{\text{tip}} > z_3 \end{cases} \quad (2)$$

where $f(z)$ is a one-dimensional quasi-static stiffness model, and z_{tip} and z_1, z_2, and z_3 are the positions of the needle tip
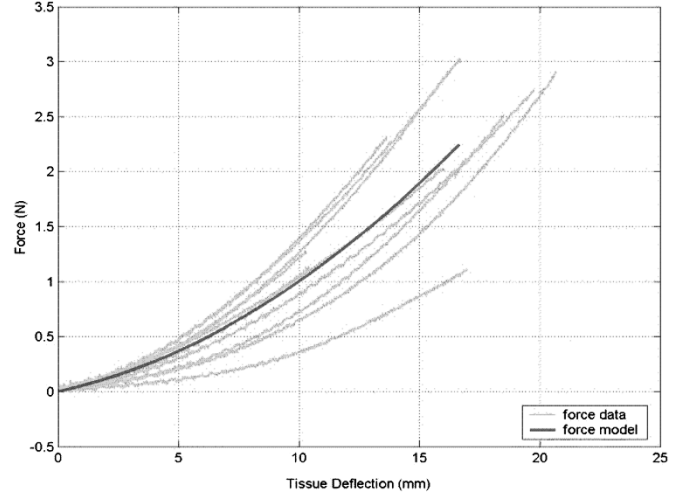

Fig. 3. Typical stiffness data for a single bovine liver before membrane puncture within a 10 cm^2 area. The curves are truncated at the deflection where puncture occurs.

and tissue surface relative to a fixed coordinate system, respectively. z_1 is the position of the undeformed tissue surface, z_2 is the position of the maximally deformed tissue surface before puncture, and z_3 is the position of the tissue surface after puncture (due to relaxation of tissue).

Biological tissue is linearly elastic for small deformations [26]. However, it is clear from our data that there is a large amount of deformation before puncture, so the force must be modeled using a nonlinear method. We first applied previous models [4], [25] to the data, but found that it was best fit by a second-order polynomial of the form

$$f(z) = a_1 z + a_2 z^2. \quad (3)$$

This is likely because we fit the data to the deflection at puncture, whereas previous work used relatively small deflections or different geometries. The intercept is zero because the force is zero before the needle contacts the surface. The data and average model are shown in Fig. 3. For Liver 1, a_1 and a_2 were 0.0480 N/mm and 0.0052 N/mm^2, respectively. For Liver 2, a_1 and a_2 were 0.0020 N/mm and 0.0023 N/mm^2, respectively. The parameter a_1 should tend to be related to the small deformation linear response, but they are significantly different for the two livers we tested. A likely explanation for this is the presence of vessels directly beneath the surface. For both parameters, each liver is likely to have variations in stiffness over a surface area due to the presence of internal structures (as shown in Fig. 1(b)). The r^2 value for Liver 1 was 0.88, and the r^2 value for liver #2 was 0.98. The second liver model was a better fit because the data for Liver 2 was recorded over and area of 5 cm^2, whereas the data for Liver 1 was recorded over an area of 10 cm^2.

We also measured the maximum deflection and force before puncture, and the drop in force after puncture. Based on 19 measurements of needle insertions into the two livers with the capsule intact, the maximum force before puncture averaged 2.3040 N (standard deviation 0.8286 N), occurring at a needle depth (corresponding to z_2) of 16.6514 mm (standard deviation 3.5470 mm). This maximum force is followed by a sudden drop in force to an average of 0.6579 N (standard deviation 0.5638 N). The large standard deviations provide evidence of
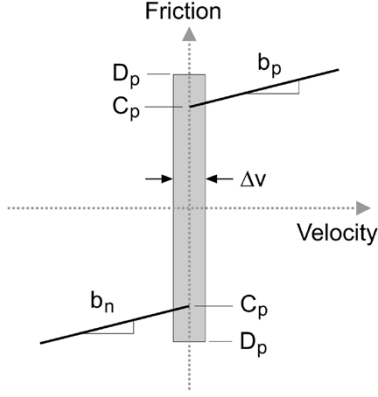
Fig. 4.   Modified Karnopp friction model (adapted from [27]).

the large variability of material properties due to inhomogeneity of a single liver.

C. Friction Forces

The purpose of this experiment was to measure friction forces during needle insertion, independent of other sources of force, such as tissue stiffness and cutting. The friction force occurs along the length of the needle inside the tissue, and is due to Coulomb friction, tissue adhesion and damping. Our model and data analysis technique is motivated by the work of Richard *et al.* [27], who modeled the friction between sets of solid materials and generated a corresponding haptic virtual environment. Armstrong-Helouvry *et al.* [28] provide an extensive survey of friction models. We selected the Karnopp friction model [29], which includes dynamic friction and static friction within a "dead zone" near zero velocity. We allow for asymmetric friction values for positive and negative velocities, as well as damping (viscous friction). There exist more sophisticated models, including the Stribeck effect [30], where the value of the friction force decreases as velocity increases at low velocities, and the Dahl model [31], which includes presliding displacement. However, the Karnopp model captures the prominent frictional effects during needle insertion. The subtle effects of the Stribeck effect and Dahl model could not be captured because low velocity data is not used in the analysis, for reasons explained later in this section.

The modified Karnopp friction model (Fig. 4) is described by

$$F_{\text{friction}}(\dot{z}, F_a) = \begin{cases} C_n \text{sgn}(\dot{z}) + b_n \dot{z}, & \dot{z} \leq -\Delta v/2 \\ \max(D_n, F_a), & -\Delta v/2 < \dot{z} \leq 0 \\ \min(D_p, F_a), & 0 < \dot{z} < \Delta v/2 \\ C_p \text{sgn}(\dot{z}) + b_p \dot{z}, & \dot{z} \geq \Delta v/2 \end{cases}$$
(4)

where C_n and C_p are negative and positive values of dynamic friction, b_n and b_p are negative and positive damping coefficients, D_n and D_p are negative and positive values of static friction, $\dot{z}$ is the relative velocity between the needle and tissue, $\Delta v/2$ is the value below which the velocity is considered to be zero, and F_a is the sum of nonfrictional forces applied to the system (which includes inertial effects and force due to elasticity of the tissue during any presliding displacement of the liver).

Given this model, the next step was to acquire force data for a range of needle velocities. The robot was programmed to move the needle in a sinusoidal motion, with a frequency of 0.2 Hz and amplitude of 20 mm/s. Data was acquired over 10 cycles at three different locations on a 25-gram liver lobe. Repeated
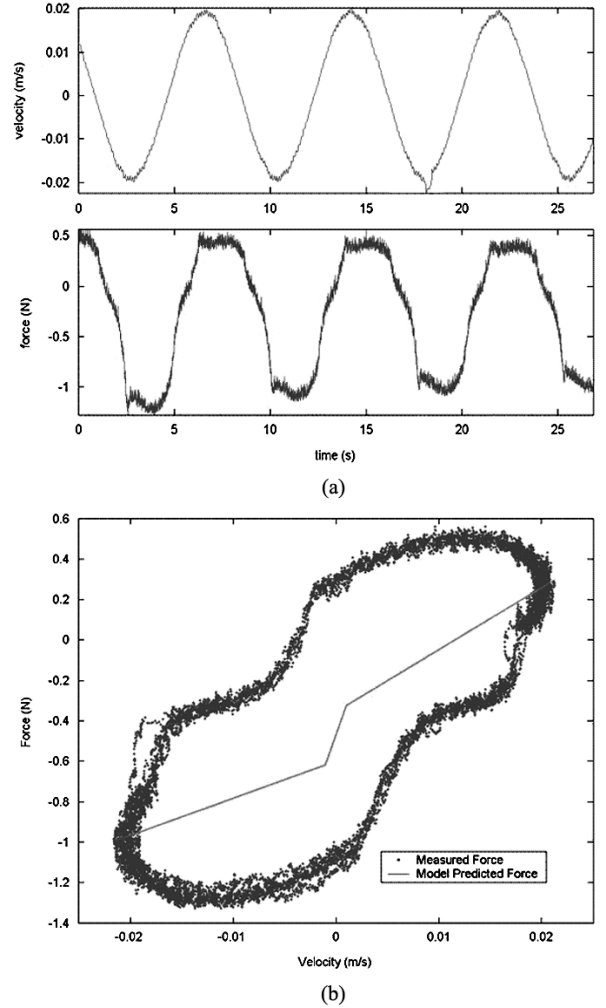

Fig. 5.   Force data for sinusoidal motion of the needle through a 3.1-cm-thick liver sample at 0.2 Hz. (a) Velocity and force versus time. (b) Force versus velocity for the original data and the Karnopp friction model with estimated parameters.

periodic motion along the same vertical line prevented cutting of new tissue, resulting in force measurements due to friction and inertia alone. The needle was passed through one lobe of liver with known thickness, so that there was always a constant amount of tissue in contact with the needle at any given time. We assumed that the capsule is ruptured upon puncture and does not provide a significant contribution to the friction forces. Qualitative observations of needle insertion with and without the capsule did not indicate a significant contribution, but this should be verified quantitatively in future work. Fig. 5 shows data acquired for a single trial.

In order to limit presliding displacement of the liver and maintain a constant thickness of tissue while the needle was in motion, an adjustable-height platform was constructed with holes that allowed the needle to pass completely through a lobe of the liver while constraining the deflection of the tissue as the needle inserts and withdraws. One negative aspect of this method is that the liver is slightly compressed between the plates and only a segment of the organ is tested. However, we performed several preliminary constant velocity insertions without these constraints and observed that the force measurements were comparable.
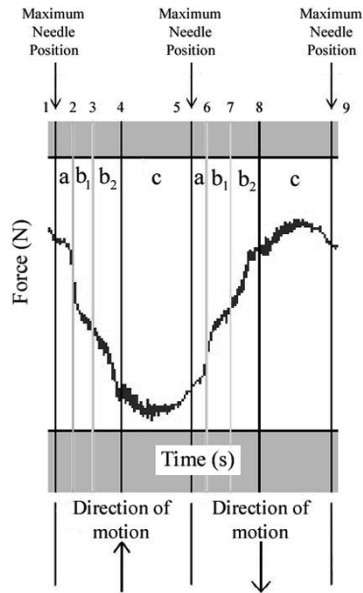
Fig. 6. Needle insertion phases, demarcated by relative velocity of needle and tissue.
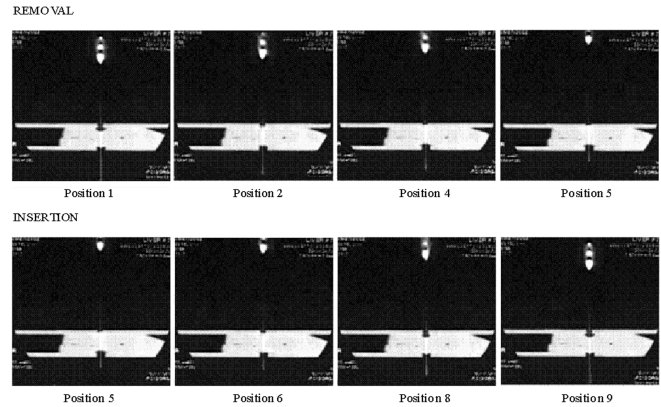

Fig. 7. CT Fluoroscopic images acquired during cyclic needle insertion into a lobe of bovine liver. To top set of images show the removal sequence and the bottom set show the insertion sequence.

Estimating the parameters of the modified Karnopp model requires knowledge of the relative velocity between the needle and the tissue. Imaging allowed us to identify portions of data with differing relative velocities between the needle and liver. Examination of CT Fluoro images revealed different phases within the force versus insertion depth profiles. In each direction of motion (insertion or removal), there are three distinct phases that correspond to varying relative velocities between the needle and the liver. Figs. 6 (force data) and 7 (image data) show the important positions and three phases of relative motion between the needle and tissue: (a) no relative motion, (b) partial relative motion, and (c) complete relative motion.

Phase (a) occurs from the time when the needle and liver are at a maximum position and velocity has just started to be nonzero (positions 1 and 5), to when the liver first contacts the plate and the bulk of its mass stops moving because of this constraint (positions 2 and 6). In phase (a), static friction dominates the behavior of the system, so the liver and needle move in unison. In this case, the velocity of the needle equals that of the liver, so the relative velocity is zero.

Phase (b) occurs from the time when the liver first contacts the plate, although there is still some tissue motion at the hole where the needle is allowed to pass (positions 2 and 6), to when the tissue has completely stopped moving and is at its maximum position (positions 4 and 8). This phase can be further segmented into (b1) and (b2). Phase (b1) occurs from the time at which the liver first contacts a plate (positions 2 and 6) to when the liver fully contacts the plate (positions 3 and 7). Phase (b2) occurs from this time (at which the liver fully contacts a plate although there is still some tissue motion through the hole), to when the tissue has completely stopped moving and is at its maximum position (positions 4 and 8). During phase (b), the portion of the liver not constrained by the plate (at the hole where the needle passes through the plate) is still in motion. In this case, the velocity of the liver is smaller than that of the needle, which results in some relative velocity between them.

Phase (c) represents the period between the time when the liver stops moving to the time when the direction of the needle (the sign of the velocity) changes. In phase (c), the tissue is no longer moving, resulting in a relative velocity equaling that of only the needle, so that phase (c) is completely dominated by the dynamic friction. For the purpose of modeling, only the data with known relative velocity are used to compute the coefficients of static and dynamic friction and damping.

As the first step toward estimating the parameters of the friction model, we segmented the data into the three phases described above. This segmentation was performed manually, by observing the images and matching the time stamp on the images with the timing of the data. We note that manual segmentation was required because automatic tracking of the liver and needle in the image would not be accurate with this experimental setup. The Toshiba Aquilion CT Fluoro™ machine acquires four simultaneous 0.5-mm slices in every $1/2$-s rotation of the gantry. These four slices are converted into three simultaneous images on the display. One image represents the slice just before the target, one is the slice right after the target, and one image combines two slices for a high-resolution view of the target. The needle is often only partly visible in the combined center image. Another limitation is that the device is not sensitive enough to pick up fine tissue details, only some major blood vessels in the viewing field. This is because the contrast of the view must be adjusted to minimize the presence of artifacts from the metal in the slice. Thus, it is difficult to automatically segment and measure needle velocity using image-processing techniques. However, it is sufficient for manual segmentation because the human eye easily identifies relative tissue and needle motion. Other imaging technologies are not appropriate for these experiments; X-ray imaging requires implanted fiducials, which change the mechanical properties of the tissue.

To obtain the coefficients of static friction, data corresponding to phase (a) was used. Velocity was assumed to be zero around a band of 0.005 mm/s ($\Delta v/2$, which was determined by the boundary of phase (a)). The static friction parameters D_p and D_n were determined by averaging the positive and negative data, respectively, from this phase.

To determine the dynamic friction and damping coefficients, data corresponding to phase (c) was used. The position data

TABLE I
ESTIMATED FRICTION PARAMETERS FOR BOVINE LIVER

Parameter	Mean	Standard Deviation
D_p (N/m)	18.45	5.42
D_n (N/m)	-18.23	4.30
b_p (N-s/m^2)	212.31	45.70
b_n (N-s/m^2)	-293.08	30.73
C_p (N/m)	10.57	4.34
C_n (N/m)	-11.96	4.40

stored from the robot encoders was smoothed with a moving average filter, then differentiated by four-point central differencing to obtain a velocity array $\mathbf{v}$. The velocity was also smoothed, then differentiated by four-point central differencing to obtain an acceleration array $\mathbf{a}$. 100 data points were removed at the end of each array to remove boundary effects. Velocities in the array with absolute velocity less than Δv were stored as zero. The data were then separated into two arrays, $\mathbf{v}_p$ (positive velocity) and $\mathbf{v}_n$ (negative velocity), such that $\mathbf{v} = \mathbf{v}_p + \mathbf{v}_n$. $\mathbf{v}_p$ is computed by setting all the elements of $\mathbf{v}$ that are less than zero equal to zero, and $\mathbf{v}_n$ is computed by setting all the elements of $\mathbf{v}$ that are greater than zero equal to zero. Using these vectors, the measured force, $\mathbf{f}_{\text{measured}}$, can be expressed as the sum of the inertia and friction forces, given the length of contact between the needle and tissue, l:

$$\mathbf{f}_{\text{measured}} = \mathbf{f}_{\text{inertia}} + \mathbf{f}_{\text{friction}}. \qquad (5)$$
$$\mathbf{f}_{\text{measured}} = m\mathbf{a} + l(C_p\text{sgn}(\mathbf{v}_p) + b_p\mathbf{v}_p \\ + C_n\text{sgn}(\mathbf{v}_n) + b_n\mathbf{v}_n). \qquad (6)$$

Since the acceleration and mass of the needle (0.087 kg) are known, (6) can be used to solve for the friction force $\mathbf{f}_{\text{friction}}$

$$\mathbf{f}_{\text{friction}} = \mathbf{f}_{\text{measured}} - m\mathbf{a} = l(C_p\text{sgn}(\mathbf{v}_p) + b_p\mathbf{v}_p \\ + C_n\text{sgn}(\mathbf{v}_n) + b_n\mathbf{v}_n). \quad (7)$$

For data points 1 through N, the matrix form of this equation is

$$\begin{bmatrix} f_{\text{friction1}} \\ f_{\text{friction2}} \\ \vdots \\ f_{\text{frictionN}} \end{bmatrix} = \begin{bmatrix} F_{\text{measured1}} \\ F_{\text{measured2}} \\ \vdots \\ F_{\text{measuredN}} \end{bmatrix} - \begin{bmatrix} a_1 \\ a_2 \\ \vdots \\ a_N \end{bmatrix} m$$

$$= \begin{bmatrix} \text{sgn}(v_{p1}) & v_{p1} & \text{sgn}(v_{n1}) & v_{n1} \\ \text{sgn}(v_{p2}) & v_{p2} & \text{sgn}(v_{n2}) & v_{n2} \\ \vdots & \vdots & \vdots & \vdots \\ \text{sgn}(v_{pN}) & v_{pN} & \text{sgn}(v_{nN}) & v_{nN} \end{bmatrix}$$

$$\times l \begin{bmatrix} C_p \\ b_p \\ C_n \\ b_n \end{bmatrix} \qquad (8)$$

This equation is of the form

$$\mathbf{f}_{\text{friction}} = A\mathbf{x} \qquad (9)$$

and we can solve for the vector $\mathbf{x} = [C_p \ b_p \ C_n \ b_n]^T$ of unknown parameters using a least squares regression

$$\mathbf{x} = (A^T A)^{-1} A\mathbf{f}_{\text{friction}}. \qquad (10)$$

The estimated parameters obtained from this analysis are shown in Table I. The same liver was tested at 10 different points, generating large standard deviations due to variation in tissue properties at different locations in the lobe. Note that the units of the parameters provided in the table are per unit length, since they are linear in the length of the needle in contact with the tissue.

D. Cutting Forces

The cutting force is that which is necessary for the needle tip to slice through the tissue. We postulate that this force exists as a combination of cutting forces and tissue stiffness at the tip of the needle, since the needle tip compresses the tissue in front of the cuts. The cutting force is isolated by subtracting the previously determined friction force from the total force. Ideally, cutting forces will be constant, and therefore unrelated to needle depth. The relation for cutting force is given by

$$f_{\text{cutting}} = \begin{cases} 0, & z_{\text{tip}} \le z_2, \quad t < t_p \\ f_{\text{cutting}}, & z_{\text{tip}} > z_3, \quad t \ge t_p \end{cases} \qquad (11)$$

where f_{cutting} is a constant for a given tissue, z_{tip}, z_2, z_3 are the same as in (2), t is time, and t_p is the time of puncture. Equation (11) assumes that the depth of the needle tip in the tissue monotonically increases with time. For five needle insertions into a liver at 3 mm/s, the average cutting force was 0.94 N (standard deviation 0.36 N). The cutting force was calculated by subtracting the estimated friction force from the total measured force after puncture.

The primary difficulty in determining cutting forces was finding insertion data segments free of collisions with internal vessels. These internal collisions add an additional stiffness force that should not be taken into account when measuring the cutting force of the liver tissue. Because of this factor, the measured cutting forces were not quite constant, but increased slightly with insertion depth. An example of cutting forces, separated from the stiffness and friction data, is shown in Fig. 8.

E. A Complete Force Model

The model was validated by direct comparison of simulated and real data. Based on the average parameter values obtained in the previous sections, a complete model of the needle insertion force profile was created. The model and data from real needle insertions can be compared in Fig. 9. The overall shape of the model is similar to the data, although the significant variations in liver geometry and internal structure make a perfect match impossible. The major drawback of this method is that collisions with small interior structures such a blood vessels are not included in the model. These add additional peaks and stiffness forces to the data. We also make the assumption that the needle remains completely straight as it travels through the tissue; in reality there are small deflections that may affect the measured force. Despite these limitations of the model, it may be still be used for event detection and haptic simulations. For application
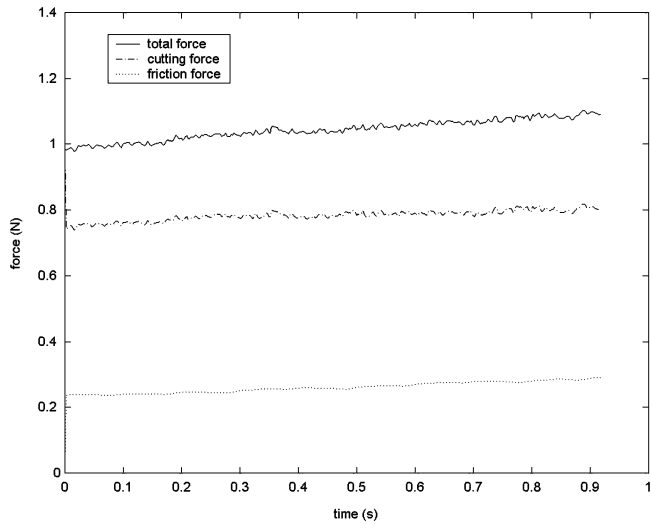
Fig. 8. Forces on the needle tip during insertion at 3 mm/s. The total force is separated into its cutting force and friction force components.
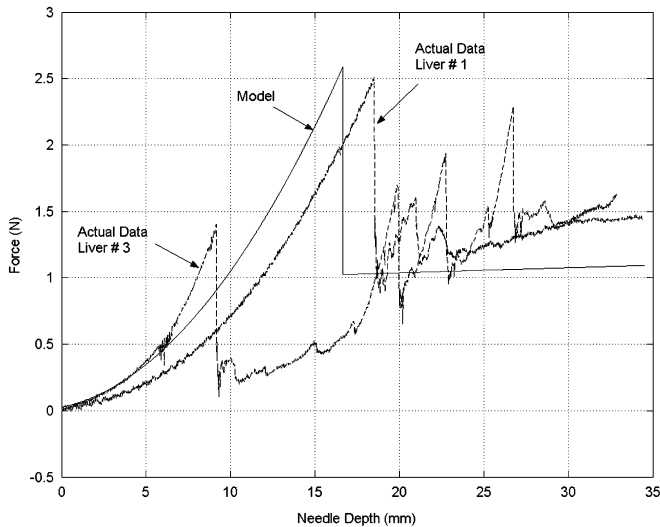

Fig. 9. The needle insertion model is compared to two insertions on real livers. Although the general shape is similar, the model cannot exactly match the data because of the wide variation in insertion forces and collisions with unmodeled internal structures.

in robot-assisted surgery, the models must be patient-specific and use preoperative images or techniques such as elastography to estimate the effect of internal structures on needle force.

IV. EFFECTS OF NEEDLE DIAMETER AND TIP TYPE ON INSERTION FORCE

The purpose of this experiment was to characterize the effect of needle diameter and geometry on insertion forces. Silicone rubber phantoms were used in order to test needle effects without the complications resulting from the inhomogeneous internal structure of real tissues. From the data, we are able to draw several conclusions regarding the effects of needle diameter and tip type on axial force and orthogonal force (needle bending).

A. Method

A cylindrical sample of silicone rubber (100-mm diameter, 40-mm height, RTV6166 from General Electric) with stiffness

TABLE II
DIAMETERS AND CUT ANGLES OF NEEDLES USED IN EXPERIMENT, WITH AVERAGE AND STANDARD DEVIATION OF THE SLOPE OF AXIAL INSERTION FORCES

Needle Type	Diameter (mm)	Average Slope (N/s)	Standard Deviation (N/s)
14° bevel	0.75	-0.263	0.010
10° bevel	1.00	-0.308	0.009
14° bevel	1.00	-0.309	0.011
20° bevel	1.00	-0.320	0.015
14° bevel	1.35	-0.420	0.017
14° bevel	1.55	-0.469	0.033
28° cone	0.59	-0.276	0.006
28° cone	0.95	-0.328	0.015
28° cone	1.55	-0.552	0.005
49° triangular	0.59	-0.171	0.006
49° triangular	0.95	-0.251	0.002
49° triangular	1.55	-0.360	0.007

properties similar to liver was used as the phantom tissue. Stainless-steel needles of various diameters and tip types were fixed to a 6-axis force sensor. Table II lists the tip types, tip angles, and diameters of the needles used in the experiment. The bevel tip is a cylinder cut through at an angle, the cone tip is a smooth cone with the peak at the center of the shaft, and the triangular tip contacts tissue with three sides of a tetrahedron (again with the tip at the center of the shaft). The force sensor has a maximum load capacity of 20 N for the x and y (orthogonal) directions and 50 N for the z (axial) direction. Voltage data from the force sensor was recorded at a rate of 250 Hz in the $x, y,$ and z directions. Calibration data was used to determine the corresponding forces. The data was smoothed using a running mean with a 100-point window. Bi-plane X-Ray was used track the position and shape of the needle. Images were recorded at 30 frames/s.

The needles were inserted into the rubber at a constant velocity of 2.65 mm/s for 7 s. Each needle then remained in the rubber for 5 s and was then extracted. This procedure was repeated three times for each of the needles in Table II. Between each trial, the rubber sample was relocated to create an un-punctured sample for each needle insertion.

B. Results

Clear phases of insertion, relaxation, and extraction can be seen in the smoothed force data. Fig. 10 shows the data acquired from a 1.00-mm bevel-tip needle. Section A is insertion and Section B is the 5-s interval where the needle is motionless. Here, the force on the needle relaxes exponentially. Section C shows the forces due to extraction. Section A reveals two effects of needle geometry, which are described in the following sections.

1) Effect of Geometry on Axial Forces: With the exception of the 0.65-mm bevel-tip needle, all of the trials revealed a linear relationship between position and axial force as the needle is inserted. The 0.65-mm needle data can be fit by second-order polynomial curve; this is most likely caused by a large amount of needle bending (discussed in the next section). When a line
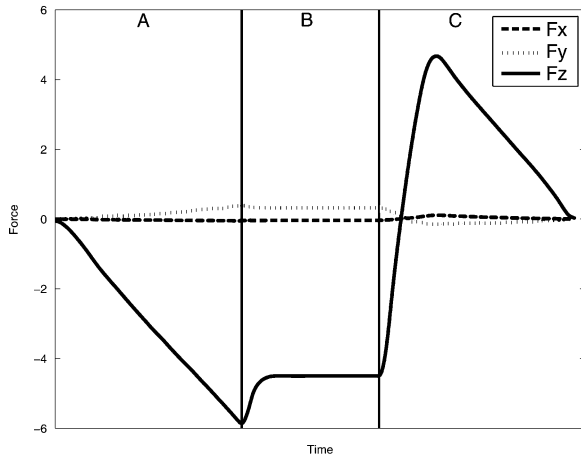
Fig. 10. Force (in Newtons) versus insertion time (corresponding to depth because of constant insertion velocity) for a 1.00 mm, 14° bevel needle, during insertion (A), holding (B), and extraction (C).

Fig. 11. Bending ratio versus needle diameter for three tip types with error bars.

TABLE III
ANOVA RESULTS FOR TYPE AND SIZE EFFECTS

Source of variation	p-value
Tip type	5.60e-13
Needle size	1.53e-17
Interaction	1.03e-5

is fit to the insertion section of the data (section A), the resulting slopes show an expected trend. As the needle diameter increases, the more the rubber is displaced and compressed in the vicinity of the needle. This increases the forces normal to the surface of the needle, leading to higher friction forces.

From Table II, it appears that the force versus position slope increases as the needle diameter increases for each of the tip types, and that the forces differ between tip types. To verify the significance of these effects, a two-factor analysis of variance (ANOVA) with $\alpha = 0.05$ (95% confidence) was performed. The factors tested were needle size and tip type (14° bevel, 28° cone, and 49° triangular tips). The needle size factor was divided into three bins: small (0.75 mm for bevel tip, 0.59 mm for cone/triangular tip), medium (1.0 mm for bevel tip and 0.95 for cone/triangular tip), and large (1.55 mm for all tip types). The input data were three trials for each combination of factors. Table III shows the p-values for three sources of variation. First, a larger needle diameter has a significantly larger force slope for all tip types. Second, there is a significant effect of tip type, with triangular tips having the lowest force, bevel tips having intermediate forces, and cone tips having the highest forces. This is a logical progression because the number of sharp edges corresponds to the ease of crack propagation and therefore cutting forces. Third, there is a significant interaction between tip type and needle size. We also attempted to correlate axial forces and bevel angle for 1.00-mm-diameter needles with bevel angles of 10°, 14°, and 20°. A single-factor ANOVA with $\alpha = 0.05$ resulted in a p-value of 0.437, indicating that there is not a significant effect of bevel angle on axial force.

2) Effect of Geometry on Needle Bending: Upon insertion, noticeable amounts of force orthogonal to the needle axis
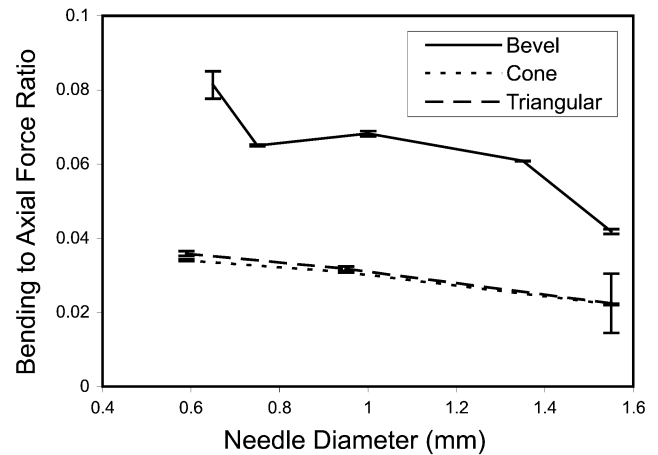
were observed, implying significant bending of the needle. This bending was verified by the X-Ray images. The standard equation for deflection of a cantilever beam is dependent on the second moment of area and, thus, the needle diameter. Based on this assumption, the amount of bending should decrease as the needle diameter increases. However, the bending forces will increase with needle diameter, due to the fact that forces are higher overall for larger needles. To get a relationship between needle diameter and bending, a ratio of maximum bending force to maximum axial force was used (the maximum force being at the instance of zero velocity).

Fig. 11 clearly shows how the bending forces tend to decrease as the needle diameter increases. However, it also shows that beveled needles bend much more than cone or triangular tipped needles. This is due to the fact that a bevel tip is asymmetric and receives higher forces on one side. This raises the question of why the cone- and triangular-tipped needles bend at all, since they are symmetric. From our data, it appears that the two symmetric needles bend because of small, random density variations in the silicone rubber. It is difficult to determine the exact locations of these inconsistencies, but their cumulative effect is evident. The fact that the data points for the beveled needle in Fig. 11 are not as consistent as those for the other two needles shows that the bevel tip needle is more susceptible to changes in the material.

From the results presented above, it is clear that the size and shape of the needle play an important role in determining the forces of needle insertion. In short, smaller needle diameters lead to less resistance force but more needle bending. Bevel tipped needles also lead to more bending where as cone and triangular pyramid tips have less and somewhat more consistent bending. (Despite this drawback, bevel tip needles are prevalent because of ease of manufacture, and the ability of the physician to rotate the needle to deliver therapy in different directions.) It can also be seen that the TP tips have less resistance force than bevel and cone tips, and that cone tips cause the highest resistance forces.

V. CONCLUSION AND FUTURE WORK

This paper presented methodologies for the measurement of stiffness, friction, and cutting forces and needle geometry ef-

fects during the insertion of needles into soft tissues. The force models developed and knowledge of geometry effects can be used in the design of virtual environments for simulation of percutaneous therapies, and the planning and execution of robot-assisted procedures.

A more complete model of the forces arising during needle insertion into soft tissues will require a combination of empirical and analytical modeling. It is likely that the most inclusive models will result from a combination of finite-element deformation modeling approaches [3] and specialized experiments to extract particular force sources (such as those presented in this paper). Future work in this field should include testing of different tissue types, the development of new testing and modeling methodologies, and multiple model (e.g., deformation and friction) integration. *In vivo* experiments or perfused organs would improve the applicability of the data, since vascular pressure, bleeding, and temperature will affect the tool-tissue interaction forces. More needles sizes and tip types should be tested, including those currently used in common percutaneous procedures. Future experiments will involve the modeling of phantom tissues of varying material properties, using automated deformation tracking.

REFERENCES

[1] P. N. Brett, A. J. Harrison, and T. A. Thomas, "Schemes for the identification of tissue types and boundaries at the tool point for surgical needles," *IEEE Trans. Inform. Technol. Biomed.*, vol. 4, pp. 30–36, Mar. 2000.

[2] I. Brouwer, J. Ustin, L. Bentley, A. Sherman, N. Dhruv, and F. Tendick, "Measuring *in vivo* animal soft tissue properties for haptic modeling in surgical simulation," *Med. Meets Virtual Reality*, vol. 9, pp. 69–74, 2001.

[3] S. P. DiMaio and S. E. Salcudean, "Needle insertion modeling and simulation," in *Proc. IEEE Int. Conf. Robotics Automat.*, 2002, pp. 2098–2105.

[4] J. Rosen, B. Hannaford, M. MacFarlane, and M. Sinanan, "Force controlled and teleoperated endoscopic grasper for minimally invasive surgery—Experimental performance evaluation," *IEEE Trans. Biomed. Eng.*, vol. 46, pp. 1212–1221, Oct. 1999.

[5] M. P. Ottensmeyer and J. K. Salisbury, "*In vivo* data acquisition instrument for solid organ mechanical property measurement," in *Proc. 4th Int. Conf. Med. Image Computing Computer-Assisted Intervention*, 2001, pp. 975–982.

[6] J. D. Andres, M. A. Reina, and A. Lopez-Garcia, "Risks of regional anaesthesia: Role of equipment—Needle design, catheters," in *Proc. 17th Annu. Eur. Soc. Regional Anaesthesia Congr.*, 1998.

[7] F. S. Azar, D. N. Metaxas, and M. D. Schnall, "A finite element model of the breast for predicting mechanical deformations during biopsy procedures," in *Proc. IEEE Workshop Mathematical Methods in Biomedical Image Analysis*, 2000, pp. 38–45.

[8] S. Nath, Z. Chen, N. Yue, S. Trumpore, and R. Peschel, "Dosimetric effects of needle divergence in prostate seed implant using ^{125}I and ^{103}Pd radioactive seeds," *Med. Phys.*, vol. 27, pp. 1058–1066, May 2000.

[9] (2004, Aug.) What are the Key Statistics for Liver Cancer?. American Cancer Society. [Online]. Available: http://www.cancer.org/

[10] K. MacLean, "The 'haptic camera': A technique for characterizing and playing back haptic properties of real environments," in *Proc. ASME Dynamic Systems and Control Division 5th Annu. Symp. Haptic Interfaces for Virtual Environments and Teleoperator Systems*, vol. DSC-58, 1996, pp. 459–467.

[11] P. E. Dupont, T. M. Schulteis, P. A. Millman, and R. D. Howe, "Automatic identification of environment haptic properties," *Presence*, vol. 8, pp. 394–411, Aug. 1999.

[12] A. M. Okamura, J. T. Dennerlein, and M. R. Cutkosky, "Reality-based models for vibration feedback in virtual environments," *ASME/IEEE Trans. Mechatron.*, vol. 6, pp. 245–252, Sept. 2001.

[13] M. Mahvash and V. Hayward. (2001, Nov.) Haptic rendering of cutting: A fracture mechanics approach. *Haptics-e, the Electronic Journal of Haptics Research* [Online], vol (3). Available: www.haptics-e.org

[14] S. P. DiMaio and S. E. Salcudean, "Simulated interactive needle insertion," in *Proc. 10th Symp. Haptic Interfaces for Virtual Environment and Teleoperator Systems*, 2002, pp. 344–351.

[15] H. Kataoka, T. Washio, K. Chinzei, K. Mizuhara, C. Simone, and A. Okamura, "Measurement of tip and friction force acting on a needle during penetration," in *Proc. 5th Int. Conf. Medical Image Computing and Computer Assisted Intervention*, 2002, pp. 216–223.

[16] R. Alterovitz, J. Pouliot, R. Taschereau, I.-C. J. Hsu, and K. Goldberg, "Simulating needle insertion and radioactive seed implantation for prostate brachytherapy," *Med. Meets Virtual Reality*, vol. 11, pp. 19–25, 2003.

[17] E. Gobbetti, "Catheter insertion simulation with co-registered direct volume rendering and haptic feedback," *Med. Meets Virtual Reality*, vol. 8, pp. 96–98, 2000.

[18] P. Gorman, "A prototype haptic lumbar puncture simulator," in *Proc. Medicine Meets Virtual Reality*, vol. 8, 2000, pp. 106–109.

[19] L. Hiemenz, "A physiologically valid simulator for training residents to perform an epidural block," in *Proc. IEEE Biomedical Engineering Conf.*, 1996, pp. 170–173.

[20] P. N. Brett, "Simulation of resistance forces acting on surgical needles," in *Proc. Inst. Mechanical Engineers*, vol. 211, 1997, pp. 335–347.

[21] V. Vuskovic, "Realistic force feedback for virtual reality based diagnostic surgery simulators," in *Proc. IEEE Int. Conf. Robotics and Automation*, 2000, pp. 1592–1598.

[22] S. Payandeh, "Force propagation models in laparoscopic tools and trainers," in *Proc. IEEE Engineering in Medicine and Biology Soc. Int. Conf.*, 1997, pp. 957–960.

[23] P. Yen, R. D. Hibberd, and B. L. Davies, "A telemanipulator system as an assistant and training tool for penetrating soft tissue," *Mechatronics*, vol. 6, pp. 423–436, June 1996.

[24] E. N. Marieb, "The Digestive System,," in *Human Anatomy & Physiology*, 5th ed. Menlo Park, CA: Benjamin/Cummings, 1997, ch. 24, pp. 920–921.

[25] D. d'Aulignac, R. Balaniuk, and C. Laugier, "A haptic interface for a virtual exam of the human thigh," in *Proc. IEEE Int. Conf. Robotics and Automation*, 2000, pp. 2452–2456.

[26] Y. C. Fung, *Biomechanics: Mechanical Properties of Living Tissues*, 2nd ed. New York: Springer-Verlag, 1993.

[27] C. Richard, M. R. Cutkosky, and K. MacLean, "Friction identification for haptic display," in *Proc. Amer. Soc. Mechanical Engineers, Dynamic Systems and Control Division*, vol. 67, 1999, pp. 327–334.

[28] B. Armstrong-Helouvry, P. Dupont, and C. Canudas De Wit, "Survey of models, analysis tools and compensation methods for the control of machines with friction," *Automatica*, vol. 30, pp. 1083–1138, July 1994.

[29] D. Karnopp, "Computer simulation of stick-slip friction in dynamical systems," *J. Dynamic Syst., Meas, Contr.*, vol. 107, pp. 100–103, Mar. 1985.

[30] V. J. Majd and M. S. Simaan, "Continuous friction model for servo systems with stiction," in *Proc. IEEE Conf. Control Applications*, 1995, pp. 296–301.

[31] P. R. Dahl, "Solid friction damping of mechanical vibrations," *AIAA J.*, vol. 14, pp. 1675–1682, Dec. 1976.

Allison M. Okamura (S'98–A'00) received the B.S. degree from the University of California at Berkeley, Berkeley, and the M.S. and Ph.D. degrees from Stanford University, Stanford, CA, in 1994, 1996, and 2000, respectively, all in mechanical engineering.

She is currently an Assistant Professor of Mechanical Engineering with The Johns Hopkins University, Baltimore, MD. Her research interests include exploration with robotic fingers, haptic display of virtual environments, teleoperation, and medical robotics.

Dr. Okamura is a member of the American Society of Mechanical Engineers. She received a 2004 National Science Foundation CAREER Award, and is a member of the IEEE Robotics and Automation Society Administrative Committee.

Christina Simone received the B.S. degree from Carnegie Mellon University, Pittsburgh, PA, in 2000, and the M.S. degree from Johns Hopkins University, Baltimore, MD, in 2002, both in mechanical engineering.

She is currently an Engineer with the Naval Surface Warfare Center, Bethesda, MD.

Mark D. O'Leary received the B.S. degree in mechanical engineering from Johns Hopkins University, Baltimore, MD, in 2003.

He is currently a graduate student in mechanical engineering at Carnegie Mellon University, Pittsburgh, PA.